Supplementary Information for

Beyond 10 MHz Organic Electrochemical Transistors for Printed Multi-valued Logic Circuits

Dong Un Lim, Sae Byeok Jo* & Jeong Ho Cho*

*Correspondence and requests for materials should be addressed to S.B.J. (e-mail: sbjo@skku.edu) or J.H.C. (e-mail: jhcho94@yonsei.ac.kr)

This PDF file includes

Details of the Experiment

Appendices S1 and 2

Supplementary Fig. S1 to S24

Supplementary Table S1 to S2

Supplementary References

Materials and methods:

Synthesis of PEDOT:PSS-O (PP2) solution: A mixture of 0.74 g of PEGME (Sigma-Aldrich) and 100 mL of PEDOT:PSS (Clevios PH) solution was allowed to react at 60 °C for 2 h. Subsequently, the mixture was allowed to cool to room temperature, and 0.5 g of imidazole was added to the mixture to neutralize the pH to 7. The prepared mixture was purified by filtration.

Synthesis of PEDOT:PSS-F (PP3) solution: To prepare this solution, 1.2 mmol of 2,2,3,3-tetrafluoropropylmethacrylate (TFPMA, Sigma-Aldrich, 99%) and 4.8 mmol of 4-styrenesulfonic acid sodium salt hydrate were dissolved in 100 mL of DI water. To this solution, 0.065 g of sodium persulfate (initiator) was added. The solution was heated to 80 °C to induce a reaction. After 24 h, the reaction was completed, and the residual sodium persulfate was removed by filtration and ion-exchange. In the prepared P(SS-coTFPMA) solution, 1.26 mmol of 3,4-ethylenedioxythiophene (EDOT, Sigma-Aldrich, 97%) was dissolved. Moreover, 0.0053 g of $Fe_2(SO_4)_3 \cdot 5H_2O$ was added to 2 mL of H_2O and 0.772 g of sodium persulfate was added to 3 mL of H_2O to initiate the polymerization reaction. After 24 h, the resultant products were purified by filtration and ion-exchange. The uniformity of the prepared solution was enhanced through sonication.

Dual-channel electrochemical transistor fabrication: On a substate, source electrodes and gate contact pads were deposited by evaporation using a shadow mask (Cr/Au = 3 nm/17 nm). Subsequently, the substrate was subjected to UV-ozone treatment. Poly(3,4-ethylenedioxythiophene)-poly(styrenesulfonate) (PEDOT:PSS) solution was spin-coated onto the substate (1000–4000 rpm), and the system was heated at 150 °C for 2 min. The PEDOT:PSS layer was patterned by conventional photolithography (AZ 5214E) and etched via reactive ion etching (RIE, FEMTO SCIENCE VITA-E). Poly(3-hexylthiophene-2,5-diyl) (P3HT) solution with a crosslinker (2,2-bis(((4-azido-2,3,5,6-tetrafluorobenzoyl)oxy)methyl)propane-1,3-diyl bis(4-azido-2,3,5,6-tetrafluorobenzoate, referred to as 4Bx) was spin-coated and photo patterned on the PEDOT:PSS layer. Au was evaporated to introduce drain electrodes on the PEDOT:PSS-P3HT vertically stacked layer. Ag/AgCl was deposited and patterned on the gate contact pad by spray-coating and used as the reference electrode. A photopatterned ion gel that covered all components served as the electrolyte. The ion gel was prepared by mixing an ionic liquid, 1-ethyl-3-methylimidazolium bis(trifluoromethylsulfonyl) imide (EMIM TFSI, Sigma-Aldrich, 98%), the poly(ethyleneglycol) diacrylate (PEG-DA, Sigma-Aldrich, M_n 575) monomer, and the 2-hydroxy-2-methylpropiophenone (HOMPP, Sigma-Aldrich, 97%) initiator (weight ratio of 21:2:1).

Device characterization: Surface images of Ag/AgCl layer were recorded using a field-emission scanning electron microscope (JEOL 7800F). The thickness and surface morphology of the PEDOT:PSS and P3HT layers were measured using an atomic force microscope (Park Systems NX10). Cyclic voltammetry curves of the PEDOT:PSS films were obtained using a Potentiostat (AMETEK VersaSTAT4) and ferrocene (Sigma-Aldrich, 98%). The electrical properties of the DuECT and logic circuits were measured using a six-arm probe station and a Keithley 4200 semiconductor characterization system.

Appendix S1. V_{ON} calculation based on cyclic voltammetry data:

The reaction to recover the conductivity of the PEDOT:PSS channel, which is lost due to reduction, is PEDOT + M^{+}:PSS^{-} -> $PEDOT^{+}$:PSS^{-} + M^{+} + e^{-}. Because the turn-on voltage of the PEDOT:PSS channel layer is the starting point of the oxidation reaction, its value can be estimated by the oxidation potential. Hence, we calculate the HOMO energy level (E_{HOMO}) of PEDOT:PSS by using cyclic voltammetry and estimate the oxidation potential through the HOMO level and standard electrode potentials.

$$E_{HOMO} = [V_{solvent} - (E_{onset\ ox} - E_{1/2(solvent)})]$$

$$\left[E^{\emptyset}_{\mathrm{H+}/\frac{1}{2}\mathrm{H2}} \right]^{\mathrm{W}}_{\mathrm{AVS}} = 4.44\ \mathrm{V}$$

$$\textit{Standard oxidation potential}\ (\textit{vs.}\ \mathrm{Ag/AgCl}) = -[E_{HOMO} + 4.44] - 0.197$$

The voltage applied to the channel in the transistor, i.e., the gate electrochemical potential, can be regarded as the sum of the gate voltage and drain voltage. The sum of the drain voltage and oxidation potential is V_{ON}:

$$V_{ON} = -[E_{HOMO} + 4.44] - 0.197 + V_D$$

Appendix S2. Numerical modeling

To calculate the changes in the turn-on voltage with the electrode area covering the channel, we estimate the difference in the electrostatic potential in the channel due to ion penetration. Because the channel thickness is considerably smaller than the channel width, a one-dimensional model is used. The boundary conditions to calculate the electrostatic potentials are set as net ion mobile speed = 0, electrolyte-channel-interface potential = drain voltage = 1 V. The electrostatic potentials are determined using the Poisson equation:

$$\frac{\partial^2 \varphi(x)}{\partial \mathrm{x}^2} = -\frac{n_e(x)}{\varepsilon_{\mathrm{s}} \varepsilon_0}$$

where x, φ, n_{e}, ε_{s}, and ε_0 represent the position along the x'-axis, electrostatic potential at position x (unit: V), electron density at position x (unit: number/cm^3), relative dielectric permittivity of the semiconductor, and vacuum permittivity (8.854×10^{-12} F/m), respectively. Solving the continuity equations and constitutive equations based on the drift-diffusion model yields the electrostatic potential as the position:

$$\frac{\partial n_{\mathrm{e}}}{\partial t} = G - R - \frac{1}{q}\frac{\partial j}{\partial \mathrm{x}}$$

$$j = q\mu_{\mathrm{e}}\left(n_{\mathrm{e}}\frac{\partial \varphi}{\partial x} + \frac{k_{\mathrm{B}}T}{q}\frac{\partial n_{\mathrm{e}}}{\partial x}\right)$$

where t, G, R, and j in the continuity equation (top) denote the time, charge generation rate, charge recombination rate, and electron current density, respectively. μ_{e} and k_{B} in the drift-diffusion equation (bottom) represent the electron mobility (unit: cm^2/Vs) and Boltzmann constant (8.617×10^{-5} eV/K), respectively. In this system, charge generation and recombination can be reasonably disregarded.

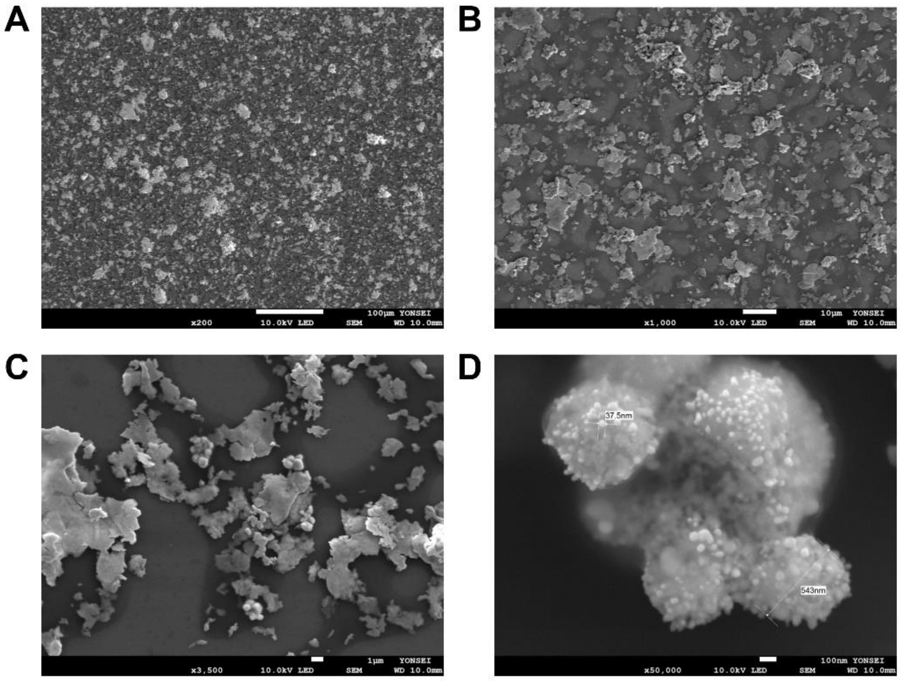

Fig. S1. (A–D) SEM images of sprayed Ag/AgCl on the gate electrode

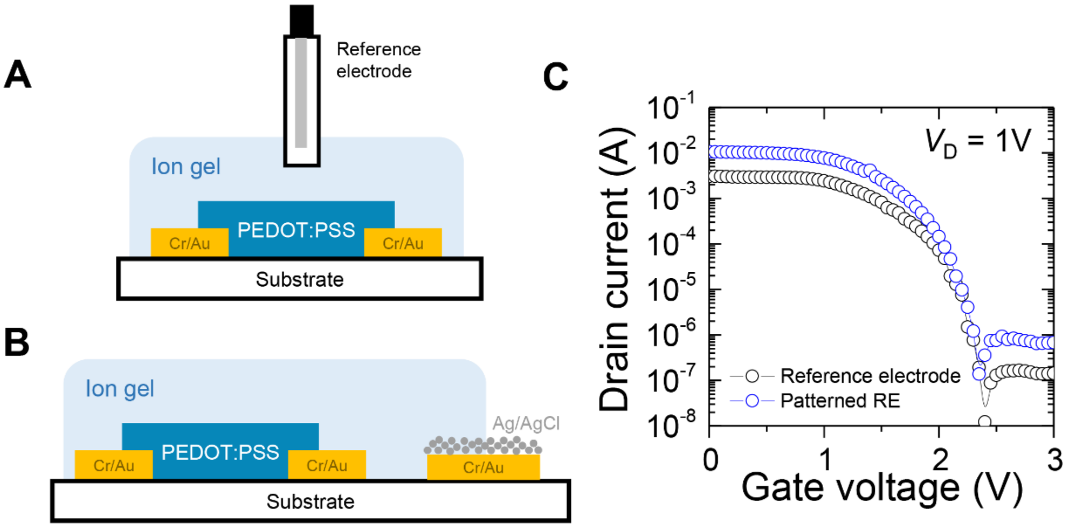

Fig. S2. Schematic of PEDOT:PSS electrochemical transistor based on a (**A**) conventional reference electrode and (**B**) sprayed Ag/AgCl electrode for gate electrode. (**C**) Transfer characteristics for each gate electrode.

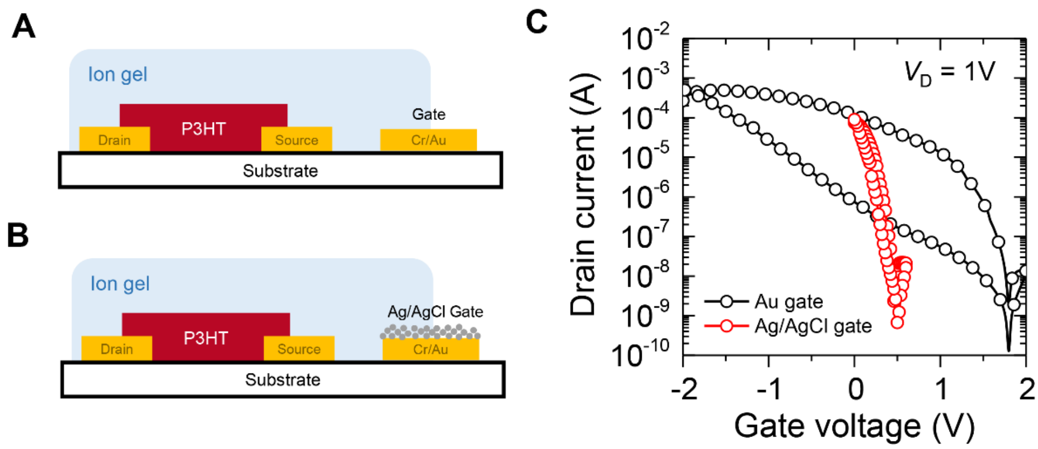

Fig. S3. Schematic of P3HT transistor based on (**A**) Au gate electrode and (**B**) sprayed Ag/AgCl gate electrode. (**C**) Transfer characteristics for each gate electrode.

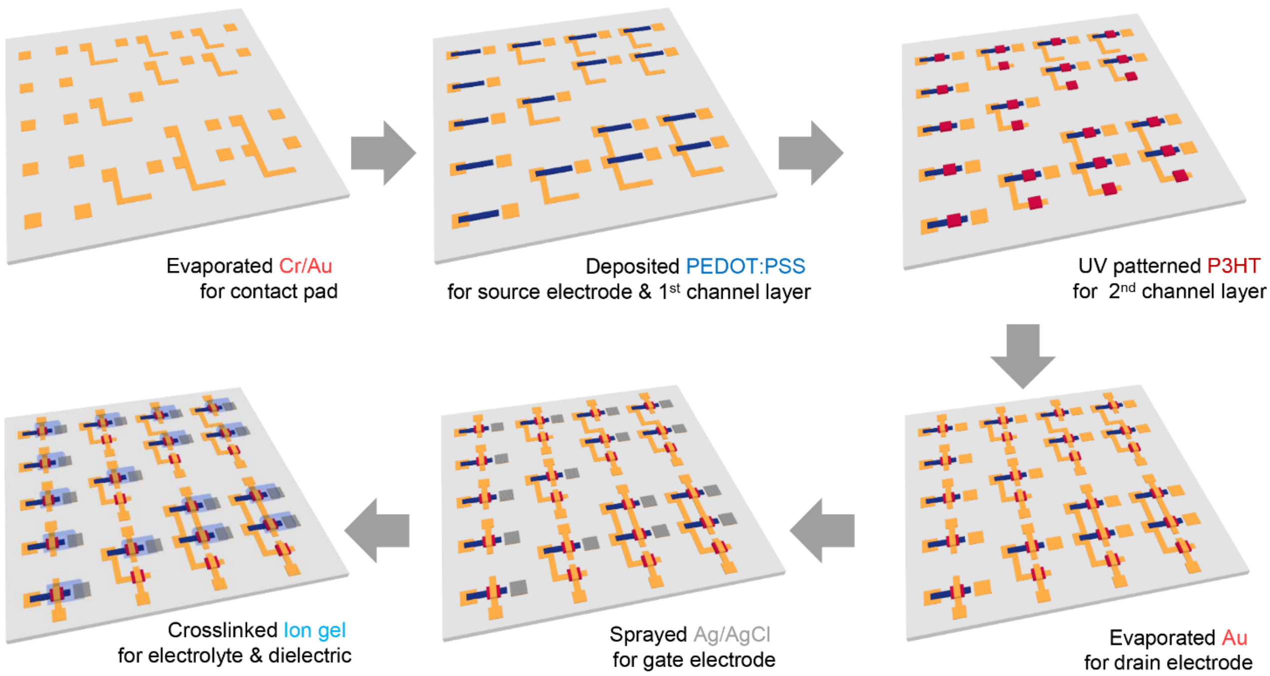

Fig. S4. Fabrication process of DuECT.

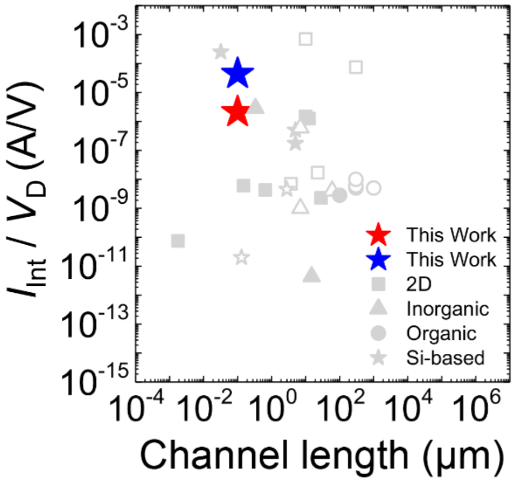

Fig. S5. Intermediate current level schematized by V_D of multivalued logic gates for the existing frameworks and DuECTs.

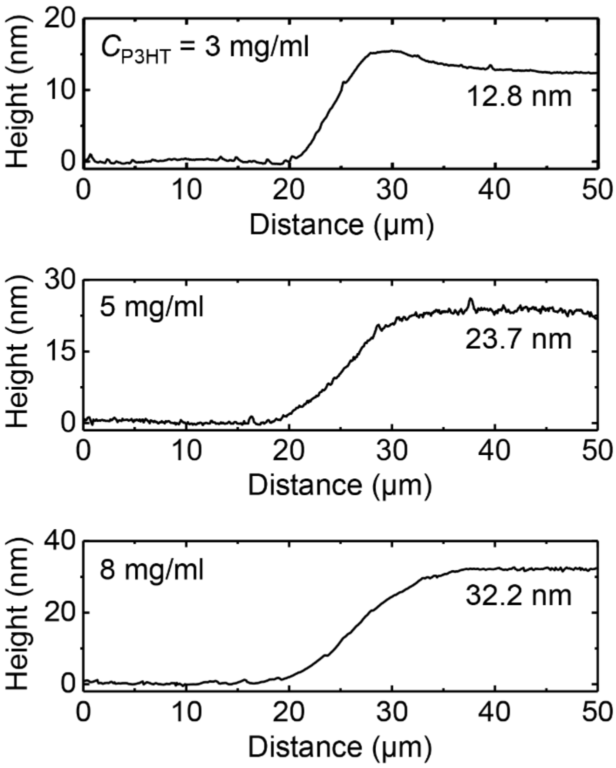

Fig. S6. Cross-section data from atomic force microscopy (AFM) indicating the thickness of spin coating layer for each P3HT concentration.

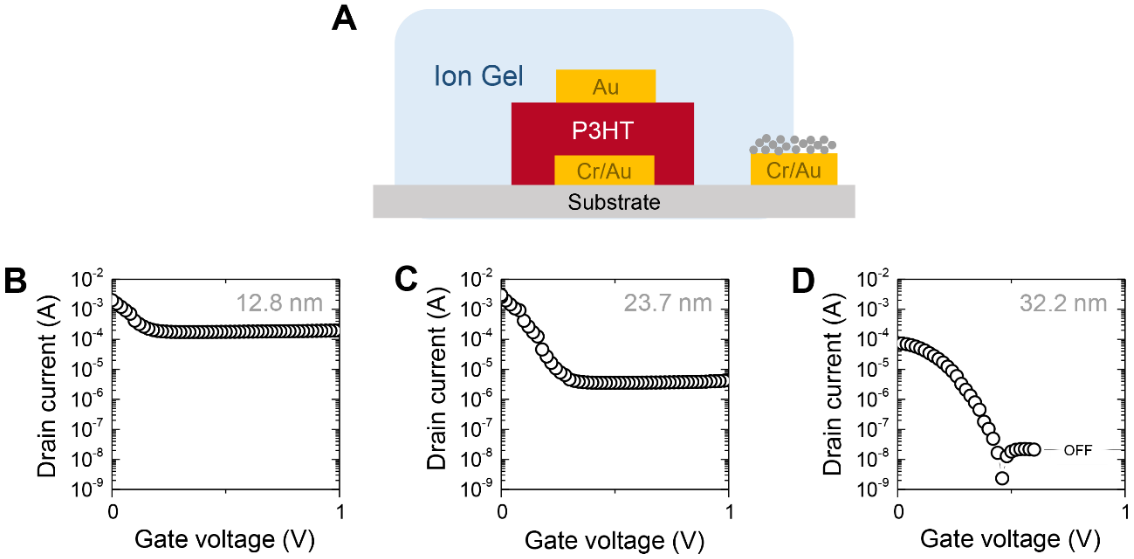

Fig. S7. (**A**) Schematic of P3HT vertical transistor. (**B–D**) Transfer characteristics for different thickness values of the P3HT channel layer.

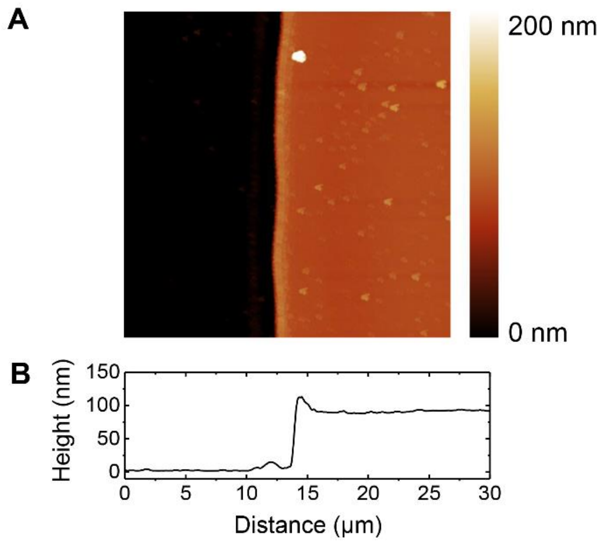

Fig. S8. (**A–B**) AFM data for thickness of the PEDOT:PSS layer.

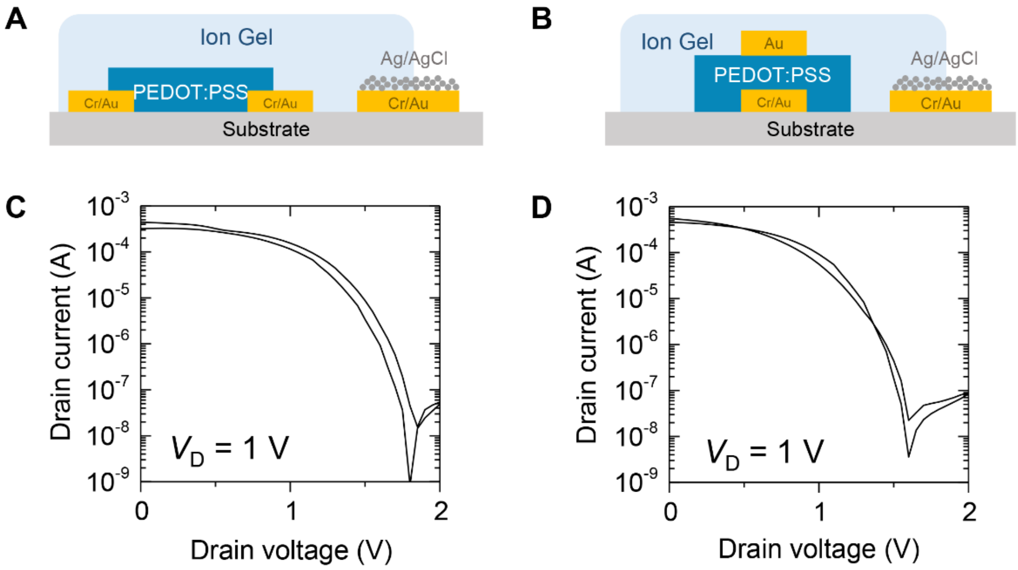

Fig. S9. Schematic of PEDOT:PSS (**A**) lateral transistor and (**B**) vertical transistor. Transfer characteristics for (**C**) lateral structure and (**D**) vertical structure.

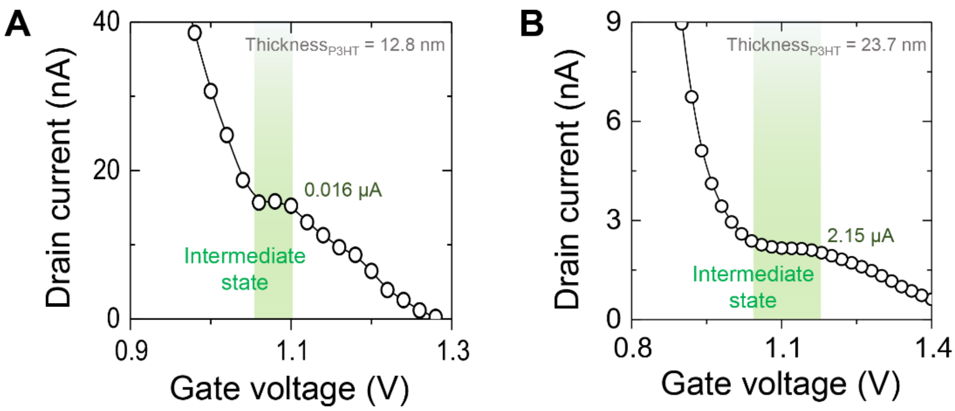

Fig. S10. Linear plot of transfer characteristics for DuECT with P3HT thickness being **(A)** 12.8 nm and (**B**) 23.7 nm.

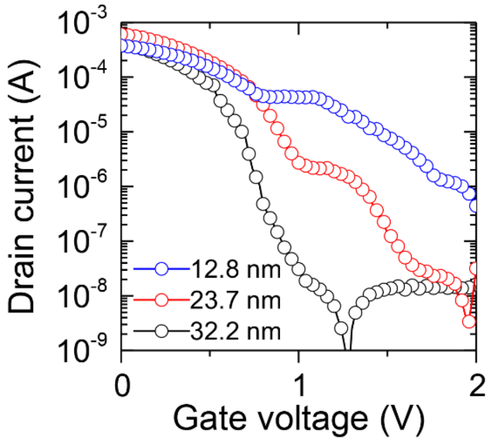

Fig. S11. Semi-log plot of transfer characteristics for different values of P3HT thickness for DuECT.

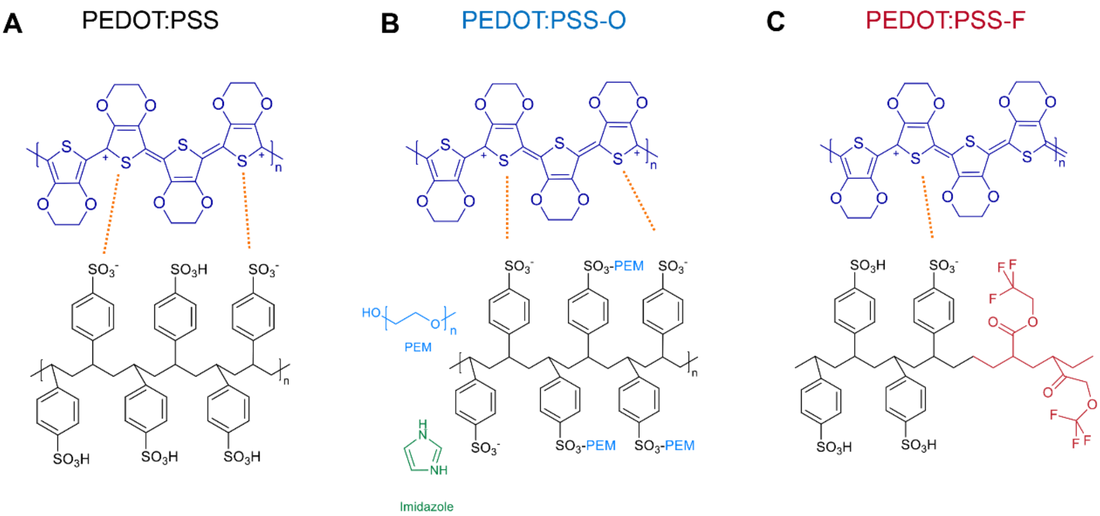

Fig. S12. Chemical structures of (**A**) PEDOT:PSS, (**B**) PEDOT:PSS-O and (**C**) PEDOT:PSS-F as channel materials in DuECTs.

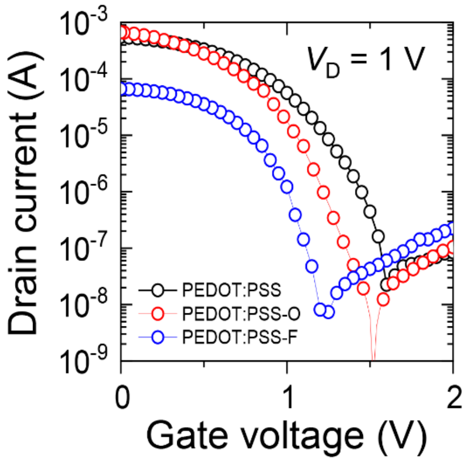

Fig. S13. Transfer characteristics of electrochemical transistors based on different PEDOT:PSS channels.

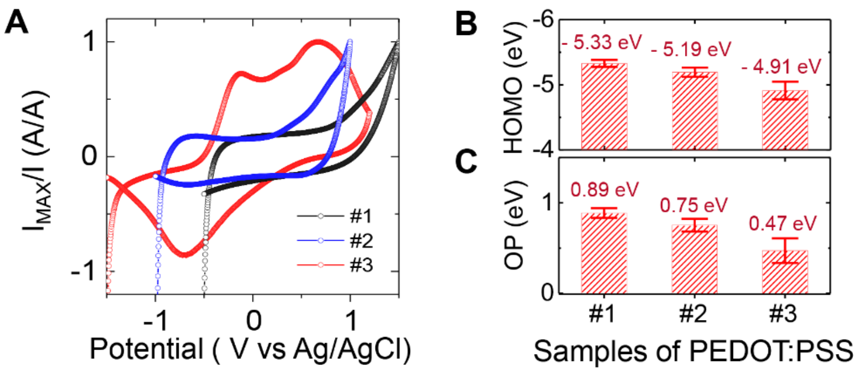

Fig. S14. (**A**) Cyclic voltammetry data of different PEDOT:PSS polymers. (**B**) HOMO level derived from cyclic voltammetry data and (**C**) oxidation potential derived from HOMO level.

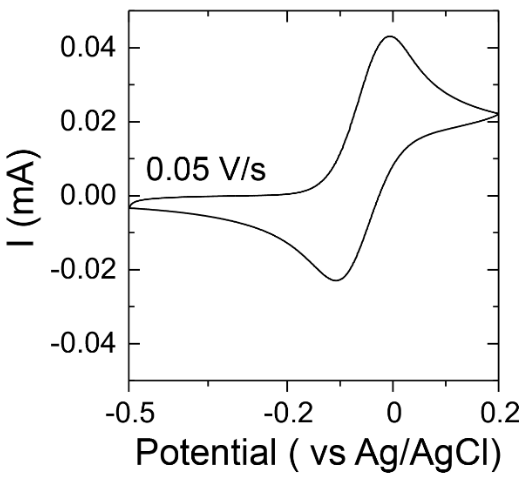

Fig. S15. Cyclic voltammetry data of the ferrocene solution.

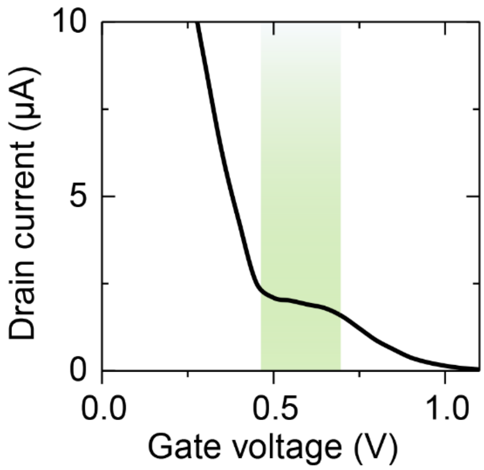

Fig. S16. Linear plot of transfer characteristics for DuECT based on the P3HT/PEDOT:PSS-F channel.

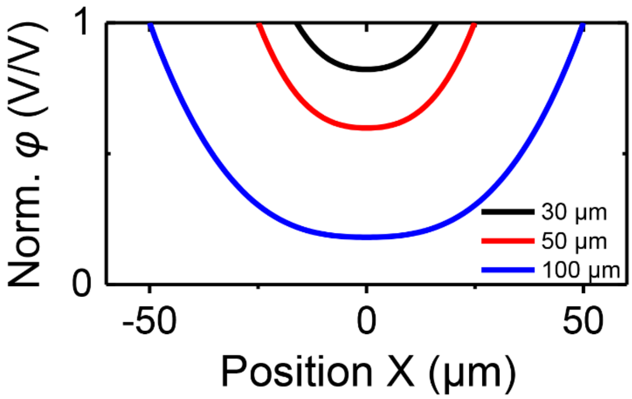

Fig. S17. Normalized electrostatic potential for dual channel under the electrode, determined through numerical calculation.

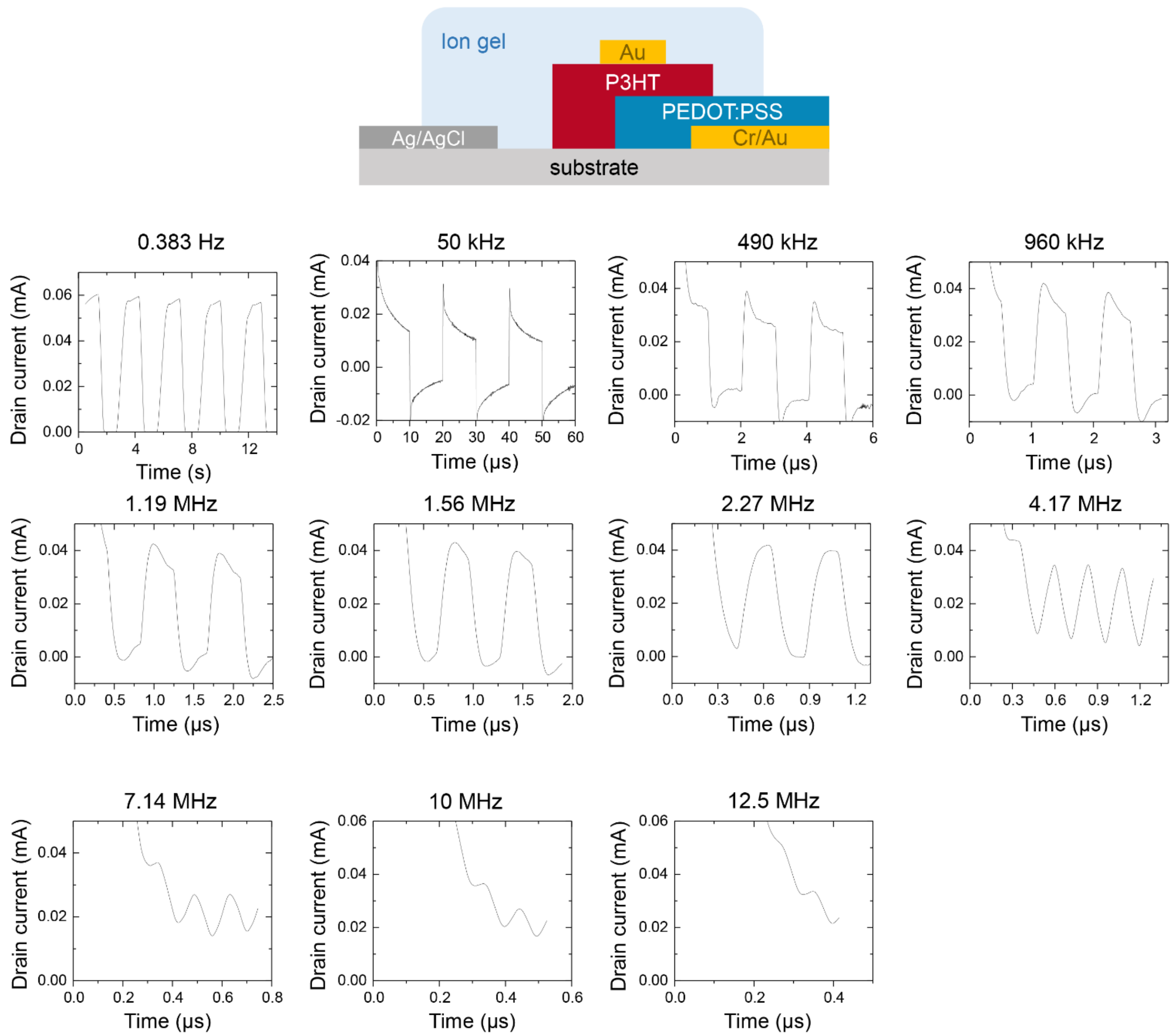

Fig. S18. Device structure and temporal responses of DuECT with various gate pulses.

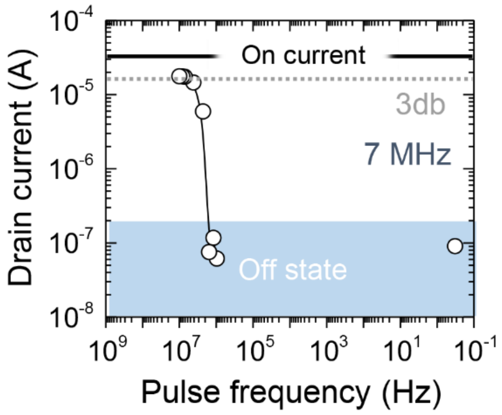

Fig. S19. Current bode plot of DuECT (unpatterned P3HT) operating at V_D = 1 V and V_G = 1 V.

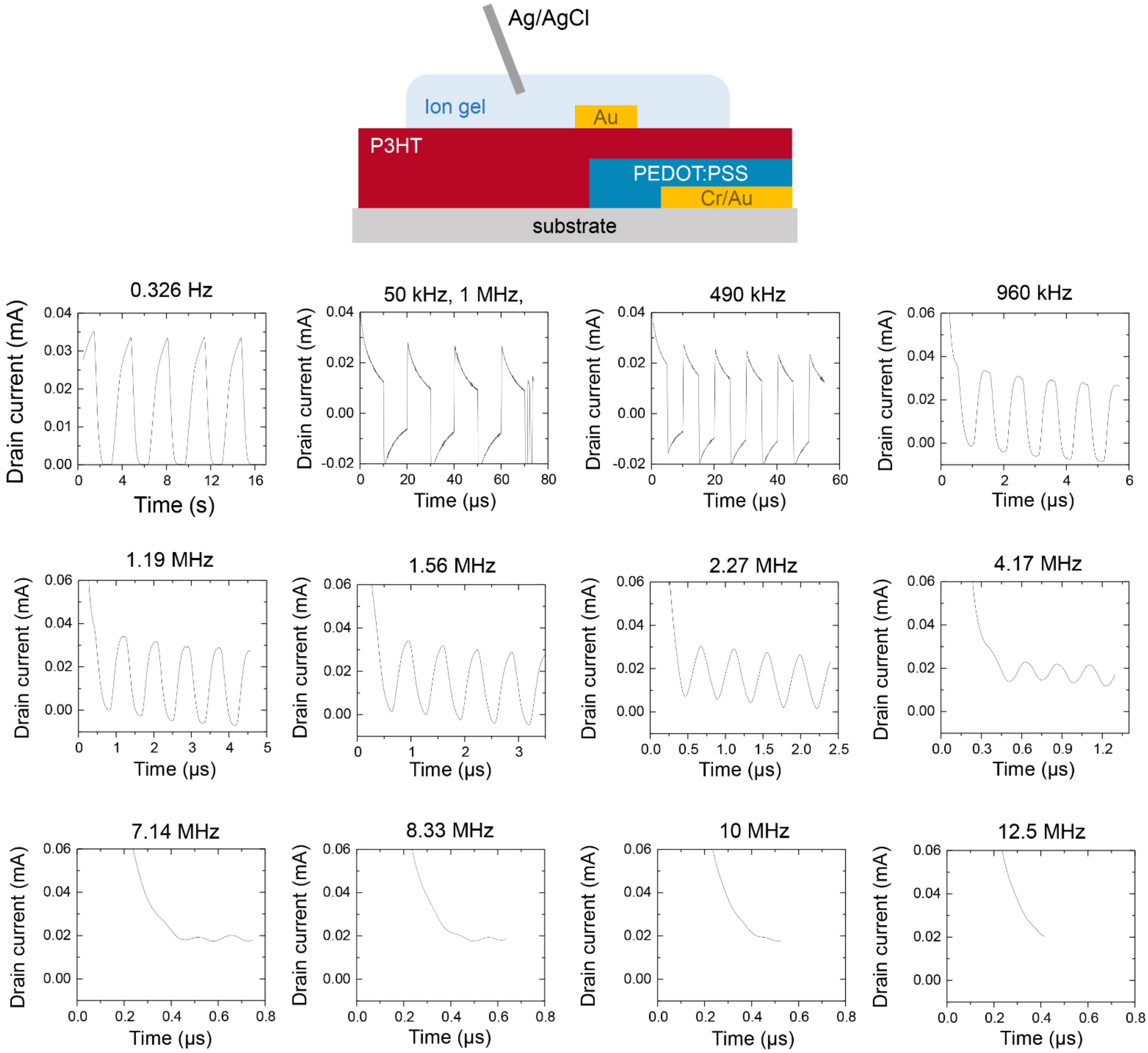

Fig. S20. Temporal responses of DuECT (unpatterned P3HT) with various gate pulses.

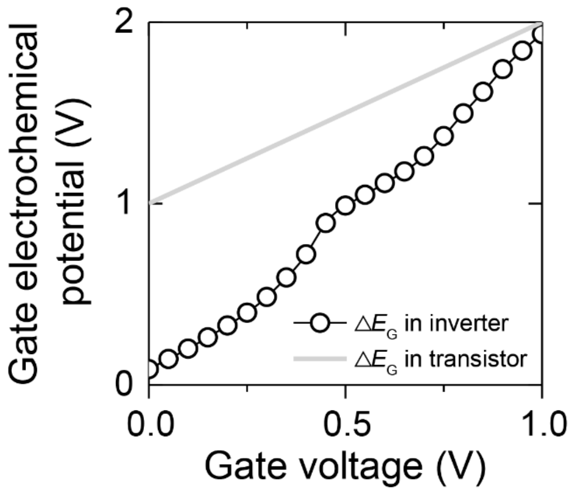

Fig. S21. Gate electrochemical potential applied to the channel on the inverter and transistor.

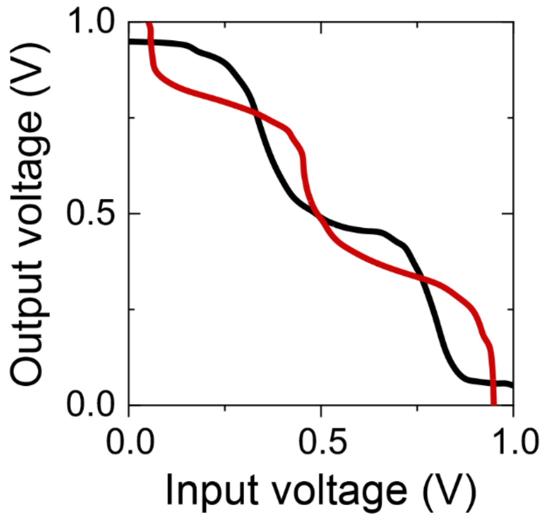

Fig. S22. Plot of symmetric in-out VTC for static noise margins of 0.1283 V and 0.0925 V.

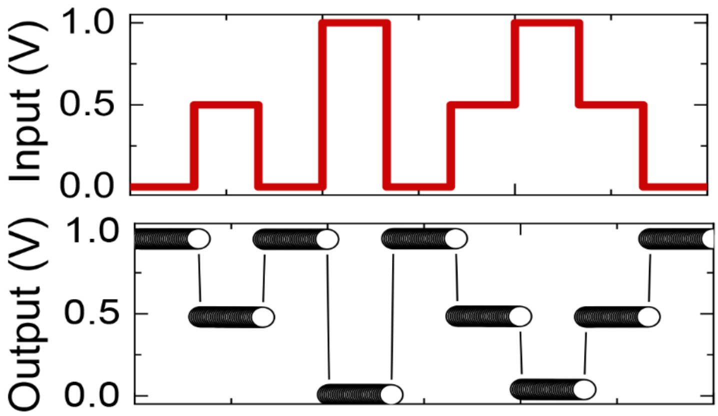

Fig. S23. Output voltages of inverter with varying input voltages.

A NMIN

	0	1	2
0	2	2	2
1	2	1	1
2	2	1	0

B NMAX

	0	1	2
0	2	1	0
1	1	1	0
2	0	0	0

Fig. S24. True tables of (**A**) NMIN and (**B**) NMAX

Table S1. Operation speeds and channel lengths in OECTs. (* measured based on Fig.s owing to the lack of accurate information.)

Year	Channel material	Electrolyte material	Gate electrode	Channel length (μm)	V_D (V)	V_G (V)	τ_{rise} or f_{-3dB}	Ref.
2004	P3HT	CyEPL	SnO_2	30	-10	-6	50 Hz	1
2005	PEDOT:PSS	NaCl	Au	50	-0.1	0.4	1 s	2
2007	P3HT	BMIM PF_6	copper	20	-1	-3	1 ms	3
2008	P3HT	EMIM TFSI		20	-1.5	-2.5	10 kHZ	4
2008	P3HT	EMIM TFSI		20	-1	-3	0.2 Hz	5
2009	P3HT	EMIM TFSI		20	-1	-3	500 Hz	6
2011	PEDOT:PSS	PBS	Pt	6	-0.5	0.4	100 us	7
2012	PEDOT:PSS	DMEM	Ag/AgCl	8000	-0.1	0.3	1 s	8
2013	CNT	EMI TCB		10	2	1.2	4.5 us	9
2013	PEDOT:PSS	NaCl	Ag/AgCl	5	-0.4	0.5	39 us	10
2013	PEDOT:PSS	NaCl	Ag/AgCl	10	-0.4	0.5	102 us	10
2014	PTHS	NaCl	Ag/AgCl	10	-0.6	-0.8	38 ms	11
2014	PEDOT:PSS	PBS	Pt or Ag	30	-0.5	0.1	1.5 ms	12
2015	PEDOT:PTHF	KCl	Ag/AgCl	10000		0.5	50 ms	13
2015	PEDOT:PSS	BMIM Otf	PEDOT:PSS	2000*	-1	2	0.2 s	14
2016	TIPS:Pentacene	NaCl		30	-0.4	1.15	0.45 ms	15
2016	p(g2T-TT)	NaCl	Ag/AgCl	10	-0.6	-0.6	420 us	16
2017	P3HT	Pyr14 TFSI		10	-1	-1	18 ms	17
2018	graphene	EMIM TFSI		5000		-4	2.4 s	18
2018	graphene	NaCl	Ag/AgCl	30	0.15	0.02	7.8 kHz	19
2018	PEDOT:PSS	NaCl	Ag/AgCl	0.45	-0.6	-0.8	1.7 kHz	20
2019	PEDOT:PSS	PBS	Ag/AgCl	30		0.3	191.2 us	21
2019	PEDOT:PSS	chitosan		30		0.3	31.7 us	21
2019	PEDOT:PSS	chitosan		12	-0.6	0.1	380 kHz	21
2019	P3HT	EMIM TFSI		0.04	-0.3	-3	1.2 kHz	22
2019	PEDOT:PSS	H_2O_2, EMEM cell	Ag/AgCl	1000	-0.2	-0.2	3.33 s*	23
2019	PEDOT:PSS	PBS	Ag/AgCl	10		0.1	1.48 ms	24
2020	PBTTT	KCl + BMIM TFSI	Ag/AgCl	20	-0.6	-0.7	3.1 s	25
2020	p(g4T2-T)	NaCl	Ag/AgCl	10	-0.6	-0.6	0.59 ms	26
2020	PEDOT:PSS	chitosan		5	-0.6	-0.4	2.9 us	27
2021	PEDOT:PSS	PBS	Au	30	0.05	0.5	0.6 ms	28

Table S2. Current levels of intermediate logic state and gate voltages multivalued logic devices. The values were measured based on peak currents in NDR and NDT devices and inverter characteristics in graphene devices owing to the lack of off-states. (* measured based on Fig.s owing to the lack of accurate information.)

Years	Device type	Material type	Channel material	Channel length (μm)	V_D (V)	V_G (V)	I_M (A)	Ref.
2011	NDR	inorganic	GaSb-InAsSb	0.333*	0.07*	X	2E-07	29
2014		2D	MoS_2, Si_3N_4	0.65*	0.512*	X	2.2E-09	30
2015		2D	MoS_2, WSe_2, graphene	0.001773*	0.8*	X	6E-11	31
2015		2D	BP, $SnSe_2$	10*	0.1*	X	1.5E-07	32
2016		2D	BP, ReS_2	28.33*	0.65*	X	1.5E-09	33
2019		2D	WSe_2, $SnSe_2$	12.5	1.8*	X	2.25E-06	34
2020		2D	BP, ReS_2, HfS_2	0.15*	0.75,1.1*	X	4.5E-09	35
2020		hybrid	HfS_2, pentacene	15*	0.45*	X	2E-12	36
2020		organic	p(NDI2OD-Se_2), P(DPP2DT-T2)	100	16*	X	4.5E-08	37
2016	NDT	2D	MoS_2, WSe_2	3.7*	1	0.31*	7E-09	38
2016		2D	graphene	10*	0.1	6.43*	7ua/um	39
2016		2D	SnS_2, WSe_2	22.67	10	-15*	7.5nA/um	40
2017		silicon	silicon	2.8	0.3	-0.25*	1.35E-09	41
2018		organic	a-6T, PTCDI-C_8	300	10	2.68*	5E-08	42
2018		organic	a-6T, PTCDI-C_8	300	-10	-7.37	6E-08	42
2018		organic	a-6T, PTCDI-C_9	300	60	-42	6E-07	42
2018		2D	graphene, R6G	300	1	10*	0.000075	43
2019		organic	DNTT, PTCDI-C_{13}	1000*	-20	-29*	1E-07	44
2019	parallel connection	inorganic, 2D	IGZO, $ReSe_2$	7, 30*	1	-1*	6E-07	45
2019		inorganic, 2D	IGZO, $ReSe_2$	7, 30*	1	1*	1E-09	45
2011	QDG FET	silicon	silicon, QD	5	0.5	1.79*	2.5E-07	46
2014		silicon	Silicon	0.032	0.6	2.2*	0.00015	47
2015		silicon	silicon, QD	5	2	0*	3.5E-07	48
2019	BTBT	silicon	silicon	0.13	0.5*	0.5*	1E-11	49
2019	edge quantization	inorganic	ZnO, Al4MP	60	1	1.4*	4E-09	50
2021	MOSSFET	organic, inorganic	IGZO, PTCDI-C_8	20	10	0	4.36E-09	51

Supplementary References:

1. Taniguchi, M. & Kawai, T. Vertical electrochemical transistor based on poly (3-hexylthiophene) and cyanoethylpullulan. *Applied physics letters* **85**, 3298-3300 (2004).
2. Mabeck, J. T. *et al.* Microfluidic gating of an organic electrochemical transistor. *Applied Physics Letters* **87**, 013503 (2005).
3. Lee, J., Panzer, M. J., He, Y., Lodge, T. P. & Frisbie, C. D. Ion gel gated polymer thin-film transistors. *Journal of the American Chemical Society* **129**, 4532-4533 (2007).
4. Cho, J. H. *et al.* Printable ion-gel gate dielectrics for low-voltage polymer thin-film transistors on plastic. *Nature materials* **7**, 900-906 (2008).
5. Cho, J. H. *et al.* High-capacitance ion gel gate dielectrics with faster polarization response times for organic thin film transistors. *Advanced materials* **20**, 686-690 (2008).
6. Lee, J. *et al.* Ion gel-gated polymer thin-film transistors: Operating mechanism and characterization of gate dielectric capacitance, switching speed, and stability. *The Journal of Physical Chemistry C* **113**, 8972-8981 (2009).
7. Khodagholy, D. *et al.* High speed and high density organic electrochemical transistor arrays. *Applied Physics Letters* **99**, 227 (2011).
8. Jimison, L. H. *et al.* Measurement of barrier tissue integrity with an organic electrochemical transistor. *Advanced materials* **24**, 5919-5923 (2012).
9. Ha, M. *et al.* Aerosol jet printed, low voltage, electrolyte gated carbon nanotube ring oscillators with sub-5 μs stage delays. *Nano letters* **13**, 954-960 (2013).
10. Khodagholy, D. *et al.* High transconductance organic electrochemical transistors. *Nature communications* **4**, 1-6 (2013).
11. Inal, S. *et al.* A high transconductance accumulation mode electrochemical transistor. *Advanced Materials* **26**, 7450-7455 (2014).
12. Campana, A., Cramer, T., Simon, D. T., Berggren, M. & Biscarini, F. Electrocardiographic recording with conformable organic electrochemical transistor fabricated on resorbable bioscaffold. *Advanced Materials* **26**, 3874-3878 (2014).
13. Gkoupidenis, P., Schaefer, N., Strakosas, X., Fairfield, J. A. & Malliaras, G. G. Synaptic plasticity functions in an organic electrochemical transistor. *Applied Physics Letters* **107**, 263302 (2015).
14. Mracek, L., Pretl, S., Syrovy, T. & Hamacek, A. in *2015 38th International Spring Seminar on Electronics Technology (ISSE).* 11-15 (IEEE).
15. Zhang, Q., Leonardi, F., Casalini, S., Temiño, I. & Mas-Torrent, M. High performing solution-coated electrolyte-gated organic field-effect transistors for aqueous media operation. *Scientific reports* **6**, 1-10 (2016).
16. Giovannitti, A. *et al.* Controlling the mode of operation of organic transistors through side-chain engineering. *Proceedings of the National Academy of Sciences* **113**, 12017-12022 (2016).
17. Thiburce, Q., Porcarelli, L., Mecerreyes, D. & Campbell, A. High performance photolithographically-patterned polymer thin-film transistors gated with an ionic liquid/poly (ionic liquid) blend ion gel. *Applied Physics Letters* **110**, 233302 (2017).
18. Kim, J. T., Choi, H., Choi, Y. & Cho, J. H. Ion-gel-gated graphene optical modulator with hysteretic behavior. *ACS applied materials & interfaces* **10**, 1836-1845 (2018).
19. Mackin, C., McVay, E. & Palacios, T. Frequency response of graphene electrolyte-gated field-effect transistors. *Sensors* **18**, 494 (2018).
20. Donahue, M. J. *et al.* High-Performance Vertical Organic Electrochemical Transistors. *Advanced Materials* **30**, 1705031 (2018).
21. Spyropoulos, G. D., Gelinas, J. N. & Khodagholy, D. Internal ion-gated organic electrochemical transistor: A building block for integrated bioelectronics. *Science advances* **5**, eaau7378 (2019).
22. Lenz, J., Del Giudice, F., Geisenhof, F. R., Winterer, F. & Weitz, R. T. Vertical, electrolyte-gated organic transistors show continuous operation in the MA cm− 2 regime and artificial synaptic behaviour. *Nature nanotechnology* **14**, 579-585 (2019).
23. Lingstedt, L. V. *et al.* Monitoring of cell layer integrity with a current-driven organic electrochemical transistor. *Advanced healthcare materials* **8**, 1900128 (2019).
24. Wustoni, S. *et al.* An organic electrochemical transistor integrated with a molecularly selective isoporous membrane for amyloid-β detection. *Biosensors and Bioelectronics* **143**, 111561 (2019).
25. Bischak, C. G., Flagg, L. Q. & Ginger, D. S. Ion Exchange gels allow organic electrochemical

transistor operation with hydrophobic polymers in aqueous solution. *Advanced Materials* **32**, 2002610 (2020).

26. Moser, M. *et al.* Ethylene Glycol-Based side chain length engineering in polythiophenes and its impact on organic electrochemical transistor performance. *Chemistry of Materials* **32**, 6618-6628 (2020).
27. Cea, C. *et al.* Enhancement-mode ion-based transistor as a comprehensive interface and real-time processing unit for in vivo electrophysiology. *Nature materials* **19**, 679-686 (2020).
28. Liu, H. *et al.* Ultrafast, sensitive, and portable detection of COVID-19 IgG using flexible organic electrochemical transistors. *Science advances* **7**, eabg8387 (2021).
29. Ganjipour, B. *et al.* High current density Esaki tunnel diodes based on GaSb-InAsSb heterostructure nanowires. *Nano letters* **11**, 4222-4226 (2011).
30. Nguyen, L.-N. *et al.* Resonant tunneling through discrete quantum states in stacked atomic-layered MoS2. *Nano letters* **14**, 2381-2386 (2014).
31. Lin, Y.-C. *et al.* Atomically thin resonant tunnel diodes built from synthetic van der Waals heterostructures. *Nature communications* **6**, 1-6 (2015).
32. Yan, R. *et al.* Esaki diodes in van der Waals heterojunctions with broken-gap energy band alignment. *Nano letters* **15**, 5791-5798 (2015).
33. Shim, J. *et al.* Phosphorene/rhenium disulfide heterojunction-based negative differential resistance device for multi-valued logic. *Nature communications* **7**, 1-8 (2016).
34. Fan, S. *et al.* Tunable negative differential resistance in van der Waals heterostructures at room temperature by tailoring the interface. *ACS nano* **13**, 8193-8201 (2019).
35. Kim, K.-H. *et al.* A multiple negative differential resistance heterojunction device and its circuit application to ternary static random access memory. *Nanoscale horizons* **5**, 654-662 (2020).
36. Jung, K. S. *et al.* Double Negative differential resistance device based on hafnium disulfide/pentacene hybrid structure. *Advanced Science* **7**, 2000991 (2020).
37. Jeon, J. *et al.* Functionalized organic material platform for realization of ternary logic circuit. *ACS applied materials & interfaces* **12**, 6119-6126 (2020).
38. Nourbakhsh, A., Zubair, A., Dresselhaus, M. S. & Palacios, T. Transport properties of a MoS2/WSe2 heterojunction transistor and its potential for application. *Nano letters* **16**, 1359-1366 (2016).
39. Kim, Y. J. *et al.* Demonstration of complementary ternary graphene field-effect transistors. *Scientific reports* **6**, 1-7 (2016).
40. Li, Y. *et al.* Anti-ambipolar field-effect transistors based on few-layer 2D transition metal dichalcogenides. *ACS applied materials & interfaces* **8**, 15574-15581 (2016).
41. Lee, S., Lee, Y. & Kim, C. Extraordinary transport characteristics and multivalue logic functions in a silicon-based negative-differential transconductance device. *Scientific reports* **7**, 1-9 (2017).
42. Kobashi, K., Hayakawa, R., Chikyow, T. & Wakayama, Y. Multi-valued logic circuits based on organic anti-ambipolar transistors. *Nano letters* **18**, 4355-4359 (2018).
43. Kim, J. B. *et al.* Photosensitive graphene P–N junction transistors and ternary inverters. *ACS applied materials & interfaces* **10**, 12897-12903 (2018).
44. Yoo, H., On, S., Lee, S. B., Cho, K. & Kim, J. J. Negative transconductance heterojunction organic transistors and their application to full-swing ternary circuits. *Advanced Materials* **31**, 1808265 (2019).
45. Yu, S. *et al.* Advanced Multifunctional Field Effect Devices using common gate for both 2D transition-metal dichalcogenide and InGaZnO Channels. *Advanced Electronic Materials* **5**, 1900730 (2019).
46. Karmakar, S., Suarez, E. & Jain, F. C. Three-state quantum dot gate fets using ZnS-ZnMgS lattice-matched gate insulator on silicon. *Journal of electronic materials* **40**, 1749-1756 (2011).
47. Karmakar, S. Ternary logic gates using quantum dot gate FETs (QDGFETs). *Silicon* **6**, 169-178 (2014).
48. Karmakar, S., Gogna, M., Suarez, E. & Jain, F. C. Three-state quantum dot gate field-effect transistor in silicon-on-insulator. *IET Circuits, Devices & Systems* **9**, 111-118 (2015).
49. Jeong, J. W. *et al.* Tunnelling-based ternary metal–oxide–semiconductor technology. *Nature Electronics* **2**, 307-312 (2019).
50. Lee, L. *et al.* ZnO composite nanolayer with mobility edge quantization for multi-value logic transistors. *Nature communications* **10**, 1-9 (2019).
51. Lim, D. U., Jo, S. B., Kang, J. & Cho, J. H. Multi-State Heterojunction transistors based on field-effect tunneling–transport transitions. *Advanced Materials*, 2101243 (2021).